Alaska Satellite Facility
News & Notes
Winter 2009, volume 6:2

Illuminating Physical Facets of an Ecological Gem: Monterey Bay, California

By John P. Ryan, Monterey Bay Aquarium Research Institute

Figure 1: Some of the more readily-visible marine life that draws upon the ecological richness of Monterey Bay; clockwise from top: a sunfish, sea lions, a humpback whale with opportunistic seabirds, and sea otters among kelp. Photos taken by E. Rienecker and J. Ryan.

Bountifully occupying the heart of a National Marine Sanctuary, Monterey Bay, California, is an ecological gem. The biological richness of this ecosystem is supported largely by transport of deep, nutrient-rich waters into the shallow sunlit zone, a process by which photosynthetic primary production is stimulated to fuel a wonderful web of life (Figure 1).

Studying a dynamic, rapidly changing environment like Monterey Bay is quite challenging. An important tool in the studies of complex coastal ecosystems is synoptic imaging by remote sensing. For example, visible- and infrared-remote sensing has shown that Monterey Bay is a hotbed for red tides, a type of phytoplankton bloom that can cause harm. Process studies integrating remote sensing with in-situ observations have explored how such blooms can develop and lead to harmful effects. It is essential in these interdisciplinary studies to understand physical forcing by the atmosphere and ocean.

By describing ocean-surface roughness, Synthetic Aperture Radar (SAR) provides a unique description relevant to understanding physical processes and their ecosystem consequences. After exploring the use of SAR in interdisciplinary studies of Monterey Bay, the author was motivated to see what the greater archive of SAR observations of this region could reveal. The Alaska Satellite Facility's (ASF) Web interface greatly facilitated searching and subsetting within the archive and batch processing with ASF's MapReady software efficiently produced a collection of more than 2,400 images for further examination.

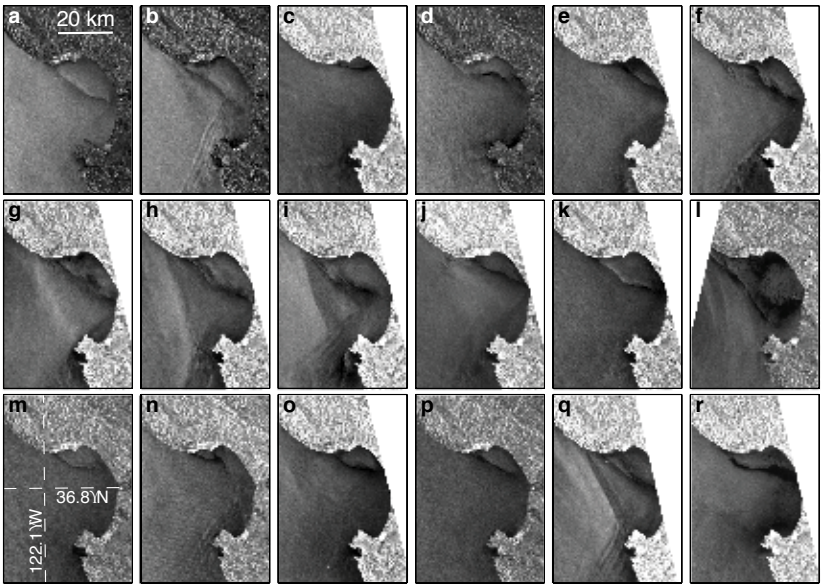

Figure 2: Examples of the most-commonly observed pattern in SAR images of Monterey Bay, a dark swath or slick, oriented NW/SE. Images are from RADARSAT-1. Recently acquired Phased Array L-band SAR images of Monterey Bay also show this pattern.

The most-frequently observed feature in the SAR archive of Monterey Bay is a distinct dark swath. Although variable in location, linearity, dimensions, and co-occurrence with other physical signals, manifestations of this signature shared the common characteristic of being oriented NW/SE across the northern bay, and most were limited to the northern bay (Figure 2). The dark swaths, representing areas of smooth sea-surface slicks, were observed in every month, except January. While 51% of the

Continued on bottom of page 3

Afterslip on Normal Faults Following Several Moderate-Sized Earthquakes on the Tibetan Plateau Observed Using InSAR

by Isabelle Ryder, University of Liverpool & Roland Bürgmann, UC Berkeley

The relatively frequent occurrence of moderate-sized seismic events makes them a good class of earthquake for exploring coseismic and postseismic deformation fields, and the associated subsurface fault geometry. This paper investigated normal faulting earthquakes that occurred during the past few years in different parts of the Tibetan Plateau. Measurements of the coseismic and post-seismic deformation fields for these events were made using Interferometric Synthetic Aperture RADAR (InSAR) allowing comparison between events. In particular, the spatial relationship between coseismic and postseismic slip was explored, and the time dependence of postseismic displacements. The earthquakes studied had magnitudes between 6.0 and 7.2. A combination of C-band SAR data from the European Space Agency's Envisat satellite and L-band data from the Japanese Advanced Land Observing Satellite (ALOS) were used in this study.

Clear surface-deformation maps were obtained for the coseismic phase of seven normal faulting earthquakes. In most cases, the coseismic-fault traces are curved, suggesting curvature of the rupture surface at depth. Detailed modeling of the observed displacement using curved faults should yield information on subsurface structure. The figures (Figure 3 and 4) highlight the January 2008 Nima-Gaize event that was modeled using planar surfaces for the mainshock and largest aftershock. Although the obtained slip model gives a very good fit to the five coseismic interferograms (Figure 3), there is a small, but systematic, residual in the images, which is believed to be a consequence of neglecting the curved geometry of the Earth. For five of the seven earthquakes studied, including the Nima-Gaize earthquake, interferograms reveal continued deformation in the months following the coseismic rupture. In every case, the observed

Continued on page 3

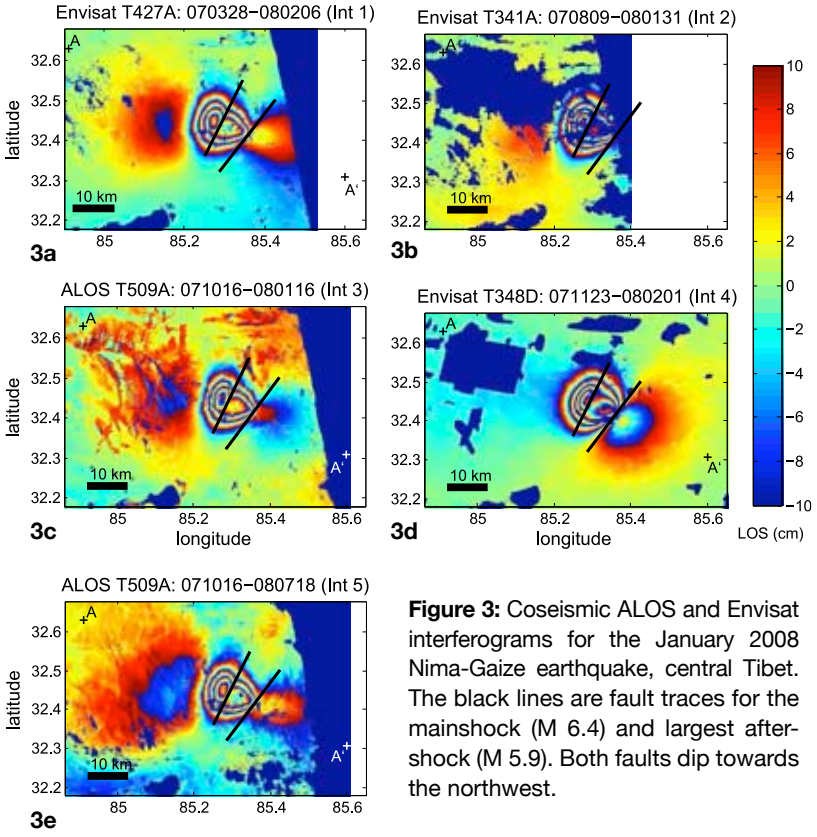

Figure 3: Coseismic ALOS and Envisat interferograms for the January 2008 Nima-Gaize earthquake, central Tibet. The black lines are fault traces for the mainshock (M 6.4) and largest aftershock (M 5.9). Both faults dip towards the northwest.

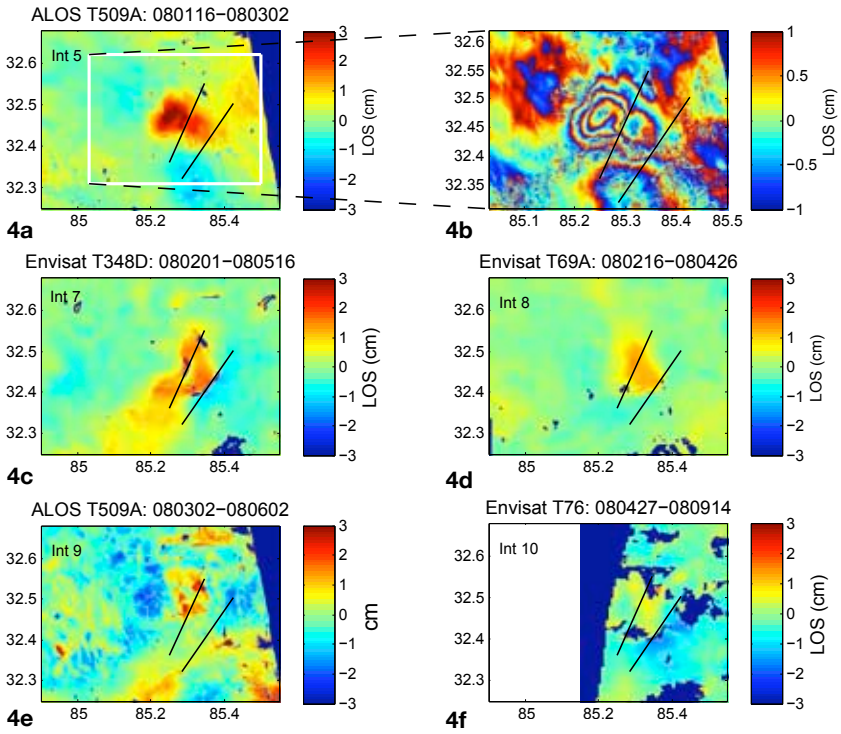

Figure 4: ALOS postseismic interferogram for the January 2008 Nima-Gaize earthquake showing surface deformation between one week and 1.5 months after the mainshock rupture. On the left is the unwrapped interferogram and on the right is a wrapped version showing the similarity with the corresponding coseismic interferogram (Figure 3c). This similarity suggests that afterslip occurred on the same fault surfaces as for the coseismic ruptures.

postseismic-surface deformation is interpreted as localized afterslip on or near the fault surfaces that slipped initially. The afterslip for each earthquake has its own unique signature. For the Nima-Gaize earthquake, both the initial rupture and the afterslip occurred on a pair of synthetic fault planes (Figure 4). For the March 2008 Yutian earthquake, there is significant afterslip concentrated towards the ends of the initial rupture, at shallow depth. The afterslip for the August 2008 Zhongba County earthquake occurred on both the coseismic rupture surface and another surface offset by a few kilometers. For the Nima-Gaize and Yutian earthquakes, sufficient data exists to create a time series of postseismic-surface deformation and can assess the time dependence of the afterslip. In both cases, rapid motion during the first couple of months gives way to a slower rate of deformation during the ensuing few months and by about 9 months after the coseismic rupture; most of the deformation has run its course. For the Nima-Gaize event, the total afterslip represents about 10% of the initial coseismic moment.

Also of interest is the exploration of rheological properties of the mid-to-lower crust, particularly in the light of the ongoing debate about the mechanical nature of the crust in Tibet. Another advantage of studying dip-slip earthquakes is that for such events, the deformation fields for localized afterslip and distributed viscoelastic relaxation look very different (unlike the case of strike-slip earthquakes, where the two mechanisms yield very similar surface-displacement patterns). Thus far, no evidence is seen in the postseismic deformation field of the events for distributed viscous flow at depth. For central Tibet, a lower bound of 5 x 1017 pascals can be placed on the viscosity of the lower crust and continued observation should allow for improvement on this constraint.

Continued from front page

images were from the months of June through October, 74% of the slicks were observed during these months, suggesting more-frequent occurrence during summer and fall.

Near-concurrent observations from visible- and infrared-remote sensing help to understand the nature of this environmental structure. In the example shown (Figure 5a), the slick marked the outer margin of a thermal front (Label F). Frontogenesis resulted from the flow of cold, recently upwelled waters, into the bay where resident waters were much warmer (Figure 5b). The frontal zone was also evident in ocean color (Figure 5c) and the region inshore of the front hosted a red-tide bloom patch (arrow in Figure 5c). A process study during this period has shown that an intense bloom was retained in the northern bay, inshore of the frontal zone, through a period of energetic mixing between the bay and adjacent waters of the California Current System.

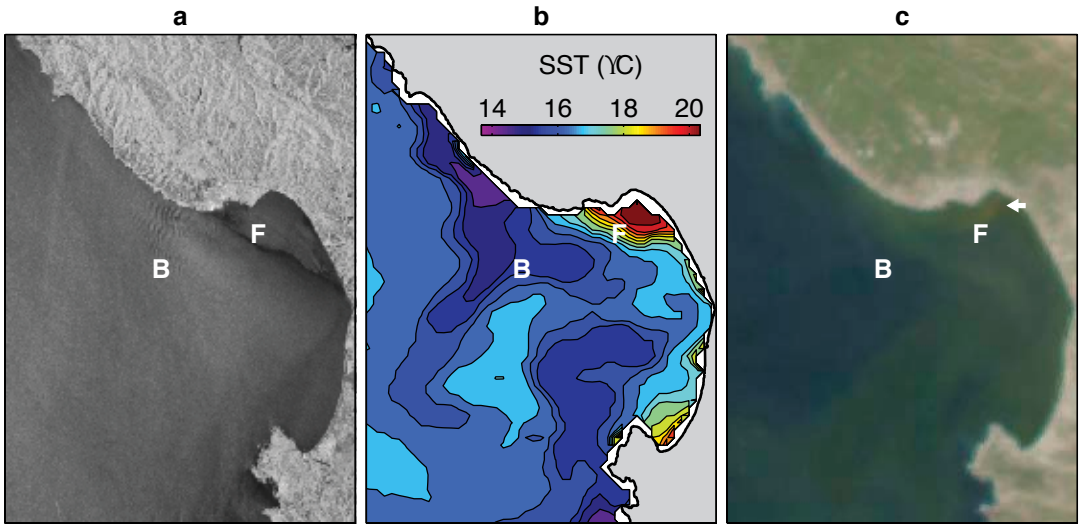

Figure 5: An example of multidisciplinary data integration with SAR: a) RADARSAT-1 image from 2 September 2004, 02:03 UTC; b) SST image from the Advanced Very High-Resolution Radiometer (AVHRR) satellite sensor, 1 September 2004, 22:18 UTC, 3.75 hours before the SAR image; c) true-color image from the Moderate Resolution Imaging Spectroradiometer (MODIS) Aqua satellite sensor, 3 September 2004, 21:45 UTC, 1.8 days after the SAR image. The AVHRR image is from NOAA CoastWatch program and the UCSC Remote Sensing Lab (R. Kudela). MODIS data were acquired through the NASA LAADS (Level 1 and Atmospheric Archive and Distribution System); processing was enabled by the MODIS Ocean Biology Processing Group and the NASA SeaDAS software development team.

Multiple observations support the conclusion that the slicks represent oceanographic processes. In case studies for which a near-concurrent sea-surface temperature (SST) image was available (n=18), the slick coincided with a thermal front having a positive onshore gradient (e.g., Figure 5). Flow of cold upwelled waters into the bay from the NW and warming of the retentive upwelling shadow of the NE bay create the typical NW/SE orientation of thermal fronts in this region, the orientation common to slicks. The relatively narrow minor-axis dimension of the slicks and their curvature over small spatial scales (e.g., Figures 2d and 2j) are consistent with oceanographic dynamics. In contrast, regional winds varied significantly in direction and intensity among the case studies, indicating that direct forcing by a specific wind pattern is not a likely

Continued on back page

Continued from page 3

cause of the slicks. One hypothesis for oceanographic processes, supported by previous case studies, is that the slicks are caused by surfactant accumulation in convergence zones. In addition to studying the causes of this common environmental structure, it is important to understand its consequences; for example, how convergent fronts influence lateral mixing, aggregation of plankton and higher trophic levels (Figure 5b), retention and export of blooms that incubate in the northern bay (Figure 5c), and settlement of marine larvae.

This research is ongoing with further examination of: (1) multidisciplinary in-situ data acquired when slicks were observed, and (2) other physical facets revealed by SAR. For example, Label B in Figure 5 indicates where a southward flow of cold waters bifurcated. Immediately north of this point was a wavelike pattern in the SAR image, which was the second most-frequently observed feature in the regional SAR archive. Is this environmental structure directly caused by oceanographic processes such as internal wave generation at a water mass confluence, or atmospheric processes such as bow-shock waves? Time, and more data, will tell.

Submissions and Subscriptions

This newsletter, published by ASF, was created to provide detailed information about special projects and noteworthy developments, as well as science articles highlighting the use of ASF data.

To receive the newsletter by postal mail, please fill out the subscription form linked to the ASF home page at www.asf.alaska.edu. Current and back issues of the newsletter can also be obtained through the ASF Web site.

Submissions to the *ASF News & Notes* and suggestions about content are always welcome. If you are interested in contributing materials, please call or send an email to the editor:

Vicky Wolf, ASF User Support
907-474-6166 | uso@asf.alaska.edu

Alaska Satellite Facility's Management

Nettie La Belle-Hamer, *ASF Director*
Scott Arko, *ASF Deputy Director*

Alaska Satellite Facility
UAF Geophysical Institute
903 Koyukuk Drive
PO Box 757320
Fairbanks, AK 99775-7320

www.asf.alaska.edu